

Surface Magnetism in Topological Crystalline Insulators

Sahinur Reja¹, H.A.Fertig¹, L. Brey² and Shixiong Zhang¹

¹Department of Physics, Indiana University, Bloomington, IN 47405

² Instituto de Ciencia de Materiales de Madrid, (CSIC), Cantoblanco, 28049 Madrid, Spain

(Dated: December 4, 2017)

We study topological crystalline insulators doped with magnetic impurities, in which ferromagnetism at the surface lowers the electronic energy by spontaneous breaking of a crystalline symmetry. The number of energetically equivalent groundstates is sensitive to the crystalline symmetry of the surface, as well as the precise density of electrons at the surface. We show that for a SnTe model in the topological state, magnetic states can have two-fold, six-fold symmetry, or eight-fold degenerate minima. We compute spin stiffnesses within the model to demonstrate the stability of ferromagnetic states, and consider their ramifications for thermal disordering. Possible experimental consequences of the surface magnetism are discussed.

PACS numbers: 73.20.At, 75.70.Rf, 75.30.Gw

Introduction – Topological crystalline insulators (TCI's) are a class of materials in which the energy bands can host non-trivial topology protected by a crystalline symmetry [1]. These systems support surface states [2] which remain gapless provided the crystal symmetry is unbroken, and are believed to present themselves in (Sn,Pb)Te and related alloys [3–8]. Interesting effects may arise when the symmetry protecting a topological band structure is broken. In topological insulators protected by time-reversal symmetry (TRS), magnetic impurities on a surface break this symmetry and form collective states [9–13], which may be understood in terms of a gap opening in the surface spectrum [14].

In contrast, TCI's are not protected by TRS, so the loss of this symmetry does not by itself energetically favor ordering of magnetic moments [15, 16]. However, a uniform magnetization can undermine one or more relevant crystalline symmetries [17, 18]. Indeed, the most common such symmetry is reflection across a mirror plane, of which there can be several. We show below that spontaneous *surface* magnetization opens a maximal gap when oriented along axes dictated by the *bulk* symmetries of the system. For a generic surface with a single mirror plane, there are two surface Dirac points at different momenta and energies [19], and in such cases at low temperature this results in a metallic, Ising-like ferromagnet, with the easy axis determined by the chemical potential μ . Importantly, the number of degenerate low-energy directions is enhanced for surfaces with further symmetries. Rotational symmetries in particular yield multiple mirror planes, and connect distinct surface Dirac cones to one another, yielding a multiplicity of easy axis directions. For sufficiently high symmetry, all the surface Dirac points may be related by symmetry operations, resulting in a fully gapped surface spectrum and a large number of groundstate orientations.

To illustrate this physics, we present detailed calculations for the (111) surface of (Sn,Pb)Te [8, 20–22], using a known model Hamiltonian [3, 23]. The (111) surface states are characterized in this system by four surface Dirac points, one at the $\bar{\Gamma}$ point and one at each of three

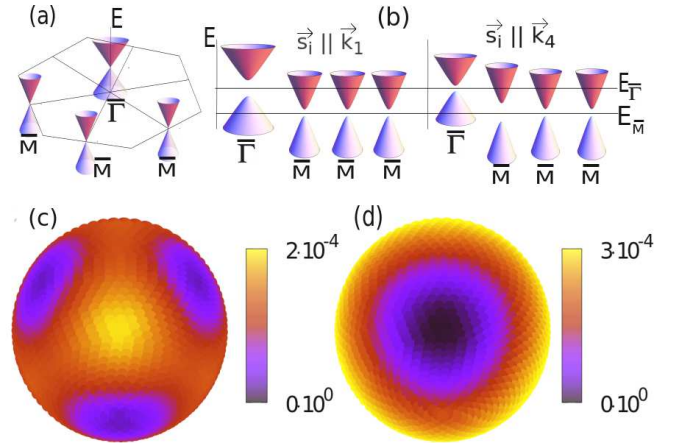


FIG. 1: (Color online.) (a) Schematic diagram of low energy states on the (111) surface. Note the three-fold symmetry. (b) Gaps induced by magnetic moments, with relative sizes depending on their orientation. (c) and (d) Total electronic energy per surface for fixed particle number atom vs. magnetization orientation on the Bloch sphere, in units of nearest neighbor hopping t . Only one hemisphere is shown in each figure, with the \mathbf{k}_1 direction represented by the center. In (c) $\mu \sim E_{\bar{M}}$; in (d), $\mu \sim E_{\bar{\Gamma}}$.

\bar{M} points [3] [Fig. 1(a).] When the system is doped by substitutional isoelectronic magnetic impurities, with μ adjusted to the bulk gap, the absence of free carriers in the volume suggests that bulk magnetism will not occur. However, it can be stabilized on the surface when it opens a gap in the surface spectrum. Moreover, the magnitude of the various gaps are sensitive to the direction of the magnetization [Fig. 1(b)]. Since the gap centers are at different energies, favored magnetization directions are determined by μ [Figs. 1 (c) and (d)]. When in the vicinity of the $\bar{\Gamma}$ Dirac point energy, there is a single easy axis, yielding an Ising ferromagnet. With μ near the \bar{M} Dirac point energies, because these points are connected by a three-fold rotational symmetry, there is a six-fold degenerate set of groundstate orientations. Remarkably, the sensitivity to μ implies that the low-energy orienta-

tions can be controlled externally by a gate.

The (111) surface is an example of how symmetry leads to a multiplicity of magnetic groundstates. This also occurs at a (001) surface, where four surface Dirac cones are supported by two distinct mirror planes. As explained below, the high symmetry leads to a potential 8-fold degeneracy of groundstate magnetization directions. Moreover, the energetic coincidence of all the surface Dirac points allows for the surface states to be fully gapped, yielding insulating behavior for a range of μ .

The existence of the degenerate magnetic groundstates should be detectable via the behavior of their domain wall (DW) excitations, which proliferate at thermal disordering transitions, or can be frozen in when the system is zero-field cooled. Furthermore, because DW's connect regions with different Chern numbers, they necessarily support bound conducting states [24]. Their energetics can also behave rather differently depending upon the placement of μ relative to the surface bands. We discuss possible effects of the DW's below.

Bulk Hamiltonian and Surface States – Our analysis employs a tight-binding Hamiltonian H_{bulk} for materials in the (Sn,Pb)Te class, which is a rocksalt structure (fcc lattice). H_{bulk} involves twelve orbitals: for each spin there are p_x, p_y, p_z states on each of two sublattices, labeled a and b , with on-site energies $m_{a,b}$ (see Supplementary Material [25]). The model represents a direct gap semiconductor with smallest gaps at the L points [$\mathbf{k} = \mathbf{k}_1, \mathbf{k}_2, \mathbf{k}_3, \mathbf{k}_4 \equiv (\frac{\pi}{2}, \frac{\pi}{2}, \frac{\pi}{2}), (-\frac{\pi}{2}, \frac{\pi}{2}, \frac{\pi}{2}), (\frac{\pi}{2}, -\frac{\pi}{2}, \frac{\pi}{2}), (\frac{\pi}{2}, \frac{\pi}{2}, -\frac{\pi}{2})$ in units of the inverse nearest neighbor separation]. For \mathbf{k} precisely at an L -point states have well-defined sublattice index (with on-site energies m_a and m_b). Adjusting $m_b - m_a$ to an appropriate value m_0 brings a and b states into energetic coincidence, forming the basis of a Dirac point at the Fermi energy.

When $m_b - m_a = m_0 + m$ with $m < 0$, there is a band inversion and associated nontrivial band topology [3], protected in this system by mirror symmetries, so that surfaces respecting any of them support gapless states [2]. Low energy forms of these may be constructed [26–28], as we describe for the specific case of the (111) surface in the Supplementary Material [25]. For this surface, there are Dirac points residing at $\bar{\Gamma}$ and each of the three \bar{M} points – as illustrated in Fig. 1 (a) – with energies $E_{\bar{\Gamma}}$ and $E_{\bar{M}}$ respectively. Note that in this situation the system has a three-fold rotational symmetry, which maps the two degenerate states at $E_{\bar{\Gamma}}$ onto one another, forming a two-dimensional representation of this rotation group. States at the three \bar{M} points form a six dimensional representation. For each Dirac point, approximate explicit forms of the the wavefunctions may be constructed [25], which can be written as eigenstates of a mirror operator $\tilde{\sigma}_1$ with eigenvalues ± 1 . Projection of H_{bulk} onto these surface states allows us to construct effective Hamiltonians in the vicinity of each Dirac point.

Magnetic Impurities and Surface Hamiltonians – It has long been known that metals in the (Sn/Pb)Te class [29–37], may be doped with magnetic ions which in some cir-

cumstances order ferromagnetically at low temperature. In these systems the magnetic ions enter substitutionally for Sn/Pb atoms, and the coupling of the magnetic moments with the conduction electrons can be understood rather well using an s – d model [38], $H_{sd} = J \sum_i \vec{S}(\mathbf{r}_i) \cdot \vec{s}_i$, where \vec{s}_i represents an impurity spin at location \mathbf{r}_i and $\vec{S}(\mathbf{r}_i)$ is the conduction electron spin density [39]. We consider the situation where the chemical potential is in a gap of the bulk spectrum, so that free carriers are not present and bulk magnetic ordering is not expected. In the TCI state, however, surface electrons couple the magnetic moments of the substitutional impurities near the surface, and may lead to ferromagnetism [40, 41]. We model this by assuming magnetic impurities are present in the system, on one sublattice, near the surface.

The explicit surface wavefunctions allow us to project the electron spin operators onto surface states for the $\bar{\Gamma}$ and \bar{M} points. As discussed in the Supplementary Material [25], the spin operators on a single (say, the a) sublattice for either the $\bar{\Gamma}$ or an \bar{M} point may be written

$$\vec{S}^{(a)} = \frac{1}{4} (u_a^2 \tilde{\sigma}_2, u_a^2 \tilde{\sigma}_1, (u_a^2 - v_a^2) \tilde{\sigma}_3). \quad (1)$$

In this expression, $\tilde{\sigma}_3$ is 2×2 matrix whose eigenvectors yield the combinations of $\tilde{\sigma}_1$ eigenstates with well-defined eigenvalues under $2\pi/3$ rotations around a bulk $\Gamma - L$ direction [25], and $\tilde{\sigma}_2 = -i\tilde{\sigma}_3\tilde{\sigma}_1$. The quantities u_a, v_a are real coefficients involving the tight-binding parameters [25]. We assume the impurity spins ferromagnetically order and treat the Hamiltonian in mean-field theory; the linear stability of the state against formation of a spin-density wave can then be checked. Projecting H_{sd} onto the subspace of surface states for a Dirac point using Eq. 1 leads to an effective Hamiltonian of the form

$$H_i \approx E_i + \alpha_i(q_2 - b_2)\tilde{\sigma}_1 + \beta_i(q_1 - b_1)\tilde{\sigma}_2 + \Delta_i\tilde{\sigma}_3, \quad (2)$$

where i denotes either $\bar{\Gamma}$ or one of the \bar{M} points, and $q_{1,2}$ represent wavevector components along the surface. (Note the relationships between (q_1, q_2) and (q_x, q_y, q_z) depend on the specific Dirac point i .) As expected on general symmetry grounds, $\alpha_{\bar{\Gamma}} = \beta_{\bar{\Gamma}}$, but $\alpha_{\bar{M}} \neq \beta_{\bar{M}}$. The offsets b_1 and b_2 are proportional to components of the impurity magnetization perpendicular to \mathbf{k}_i , while Δ_i is proportional to the component along it. The resulting spectra, $\varepsilon_i = E_i \pm \sqrt{\alpha_i^2(q_1 - b_1)^2 + \beta_i^2(q_2 - b_2)^2 + \Delta_i^2}$, provides the important observation that when the moments align along a $\Gamma - L$ direction and $\mu \sim E_i$, a gap opens in the corresponding surface spectrum that lowers its contribution to the total electron energy [14].

Numerical Studies – To test this idea we have numerically computed the electronic energy of a TCI slab with open (111) surfaces, using the tight-binding model H_{bulk} [25], and adding an effective magnetic field \vec{b} near the surface on only the a sublattice, in such a way that their coupling to the two states associated with the surface Dirac cones is the same. Our tight-binding parameters are adapted from Ref. 42, and we have verified the pres-

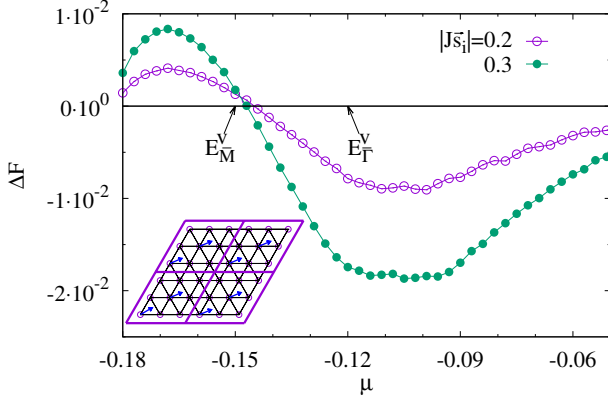


FIG. 2: (Color online.) Difference in free energy per surface atom in units of nearest neighbor hopping t , when magnetic moments are oriented in the (111) direction and in the $(1\bar{1}\bar{1})$ direction, as a function of μ , for two different strengths of $J|\vec{s}|$ in H_{sd} . E_F^V and E_M^V indicate valence band tops for $J|\vec{s}| = 0.3$ with \vec{s} in each direction respectively. Here there are 2 magnetic ions for 9 atoms on the surface in the unit cell (inset).

ence of four surface Dirac points. (Some technical details are provided in the Supplementary Material [25].) Initially we consider a slab with primitive unit cell presenting only a single site of one sublattice on the surface, and introduce a surface magnetization as described above. While this represents a relatively large density of impurities (relative to experiment), it captures the correct qualitative physics, and allows us to study a wide enough slab that the surfaces are effectively decoupled. As expected from the above discussion, among the four Dirac cones the one with largest magnetization projection along its corresponding $\Gamma - L$ direction develops the largest gap. Figs. 1 (c) and (d) illustrate the resulting total electronic energy, for $\mu \sim E_{\bar{M}}$ in (c) and $\mu \sim E_{\bar{F}}$ in (d). The energy is minimized in the former case for \vec{s} along a $\Gamma - L$ direction associated with an \bar{M} point, while in the latter minimization occurs for \vec{s} along \mathbf{k}_1 . This leads to two degenerate minima for $\mu \sim E_{\bar{F}}$ and six for $\mu \sim E_{\bar{M}}$. (Only half of these can be seen in the figures.) Analogous results are found when μ rather than particle number is fixed. As expected, the number of minimal energy states reflects the symmetry of the surface.

To further substantiate this, we also studied a more dilute magnetic moment model, in which the impurities are present only for 2/9 of the atoms of one sublattice near the surface. Fig. 2 shows the difference in Gibbs free energy of the system ($\langle H_{bulk} \rangle - \mu N$ with N the number of electrons) when the magnetic moments are oriented in the (111) direction and in the $(1\bar{1}\bar{1})$ direction, as a function of chemical potential. The results again demonstrate that energetically favored directions are determined by μ . We have also used this geometry to verify that orienting the two surface magnetic moments in different directions always raises the energy of the system, supporting our assumed ferromagnetic ordering, and that different place-

ments of the impurities in the unit cell on one of the sublattices has little effect [25]. The latter suggests that disorder in the impurity location has little impact on our results [9]. Finally we note that density of states resonances [43] that appear from vacancies and impurities in, for example, graphene, do not appear to be present for the kind of disorder we consider.

The ferromagnetic ordering may be further substantiated by considering what happens to the electronic energy when the effective field is allowed to vary spatially with some wavevector \vec{Q} along an average direction, $b_{1,2}(\mathbf{r}) = b_{1,2}^{(0)} + \delta b_{1,2} \cos(\mathbf{Q} \cdot \mathbf{r})$, $\Delta(\mathbf{r}) \equiv \Delta^{(0)} + \delta\Delta \cos(\mathbf{Q} \cdot \mathbf{r})$. To compute this we adopt as our basic Hamiltonian Eq. 2, assuming for simplicity $\alpha_i = \beta_i \equiv \alpha$, use the directions associated with q_1 and q_2 to define x and y directions on the surface, and compute the change in energy to second order in $\delta b_{1,2}$, $\delta\Delta$, and Q . Interestingly, for the valleys in which there are Fermi surfaces, this turns out to be independent of Q , as is the case for graphene [44]. Thus the spin stiffness (quadratic dependence of the energy correction on Q) comes from any valley(s) for which the Fermi energy passes through a gap. After an involved calculation (see Supplementary Material [25]), one finds a correction of the form

$$\frac{\delta E(Q) - \delta E(0)}{\mathcal{S}} = \frac{1}{2} \sum_{\mu, \nu=x,y} \rho_{\mu,\nu} Q_\mu Q_\nu, \quad (3)$$

where the coefficients $\rho_{\mu,\nu}$ are all second order in the deviations $\delta b_{1,2}$, $\delta\Delta$, and the eigenvalues of the 2×2 matrix it represents are positive [45]. This demonstrates that if the effective field from the surface magnetization has a spatial oscillation, the resulting energy increases with increasing oscillation wavevector, as should be for a ferromagnetically aligned groundstate. Note that the stiffnesses $\rho_{\mu,\nu}$ all diverge as $1/\Delta^{(0)}$ [25], a property with interesting consequences to which we will return.

(001) Surface – The (001) surface of SnTe supports gapless states that differ qualitatively from those of the (111) surface in that they involve valley admixed states [2] in the vicinity of an \bar{X} point of the surface Brillouin zone. The effective Hamiltonian for such surface states may be written in the form

$$H_{\bar{X}} = v_1 q_1 \tilde{\sigma}_1 + v_2 q_2 \tilde{\sigma}_2 + E_{\bar{X}} + \eta_1 \tilde{\mu}_x \tilde{\sigma}_1 + \eta_2 \tilde{\mu}_y, \quad (4)$$

where $q_1 = (q_x + q_y)/\sqrt{2}$, $q_2 = (q_x - q_y)/\sqrt{2}$, $\tilde{\mu}_{x,y}$ are a Pauli matrices acting on a two-fold valley space, and η_1, η_2 are phenomenological valley-mixing parameters [2]. This expression may be arrived at by explicit projection of two valleys (e.g., \mathbf{k}_1 and \mathbf{k}_4) onto (001) surface states using the approach described above. Dirac points for this Hamiltonian lie at the momenta $q_1 = \pm(\eta_1^2 + \eta_2^2)^{1/2} \equiv q_\pm$, $q_2 = 0$. Explicit forms for the two zero energy surface states at each of these points may be obtained using the same approach as for the (111) surface, and effective electron spin operators on the $j = a$ sublattice derived which couple to magnetic impurities. Assuming these are ferromagnetically aligned, in mean-field theory they add a

term of the form $\vec{h} \cdot \vec{S}^{(a)}$, where \vec{h} is the average magnetization, and induce a gap Δ at the Dirac points satisfying

$$\frac{q_{\pm}^2 \Delta^2}{4} = [\tilde{D}(h_x + h_y) - \sqrt{2}\tilde{C}(h_x - h_y)q_{\pm}]^2 + 2[\tilde{A}\eta_2 - \tilde{B}\eta_1]^2(h_x + h_y)^2 + [\tilde{D}\eta_1 + u_a^2\eta_2/\sqrt{6}]^2h_z^2,$$

where $\tilde{A} = (u_a^2 - v_a^2)/12\sqrt{6} + 4u_av_a/\sqrt{12}$, $\tilde{B} = (u_a^2 + 2v_a^2 - 4\sqrt{2}u_av_a)$, $\tilde{C} = u_a^2/2 - v_a^2$, and $\tilde{D} = (v_a^2 - u_a^2)/\sqrt{12}$. For fixed magnitude of \vec{h} , it is easy to see that there are two oppositely oriented directions that maximize Δ ; moreover, these directions are different for q_+ and q_- . Together with the four-fold symmetry that guarantees equivalent behavior for the coupled $\mathbf{k}_2 - \mathbf{k}_3$ valleys, we conclude that there are *eight* minimal energy directions for \vec{h} for the (001) surface when the Fermi energy is in the vicinity of $E_{\bar{X}}$. Furthermore, because all the Dirac cones are centered at this energy, we expect the gaps will generally overlap, so that the chemical potential may pass through all of them simultaneously. The spontaneously magnetized (001) surface then allows for *insulating* electronic behavior, in contrast to the (111) surface which for dilute magnetic impurities remains metallic.

Discussion and Speculations – We next consider some physical consequences of the surface magnetism discussed above, focusing on temperature ranges where the impurity magnetic moments may be treated classically. As mentioned above, the sensitivity of the magnetization directions for energy minima to μ should allow it to be controlled via a gate potential, which in principle would be observable in direct magnetization measurements. Another basic observation is that the gap openings induce a Berry's curvature in the surface bands, which generically induces an anomalous Hall effect. For the SnTe system with (111) surfaces we do not expect it to be quantized [17, 18], since the chemical potential typically cannot pass through a gap for all the surface Dirac species at the same time. By contrast, for (001) surfaces where the Dirac cones points are initially all at the same energy, the surface magnetization may allow all the induced gaps to overlap. With chemical potential in this gap, one does expect a quantized anomalous Hall effect [17, 18].

It is interesting to consider possible consequences of $\rho_{\mu\nu} \sim 1/\Delta^{(0)}$ as discussed above. In particular we expect that the multiple minima presented in Fig. 1 imply that there should be DW excitations in the system, with energy per unit length scaling as $\sqrt{\Delta^{(0)}}\rho_0$, with ρ_0 an appropriate average of $\rho_{\mu\nu}$'s. This remains *finite* even as $\Delta^{(0)}$ vanishes, as should happen at high enough temperature. The divergence of the spin stiffness, $\rho_0 \sim 1/\Delta^{(0)}$, reflects the fact that as the gap vanishes, the quantity $\delta E(\mathbf{Q})$ is no longer analytic in \mathbf{Q} , and in particular rises *linearly* with Q in the long wavelength limit [44], suggesting a non-local interaction among spin gradients. Presuming μ ends up at the Dirac point as $\Delta^{(0)}$ vanishes, the simplest model of the system is a clock model with long-range interactions, which in the Ising case would approach the transition with mean-field exponents [46].

For other values of μ it is possible that DW's with finite energy per unit length can be stabilized in this circumstance, but if so would not have the simplest structure [47]. In the case of the (111) surface, for $\mu \sim E_{\Gamma}$ the system presumably will undergo a second order phase transition in the Ising universality class. By contrast, for $\mu \sim E_{\bar{M}}$ case with six different minima the system could be represented by a six-state clock model. For the (001) surface and $\mu \sim E_{\bar{X}}$, an eight-state clock model is relevant. In both these cases, presuming μ does not evolve precisely to a Dirac point as the magnetization disorders and the gaps close, the phase transitions should be in the Kosterlitz-Thouless universality class [48].

We also note that DW excitations in this system may accumulate charge, both due to mid-gap states [24, 49], and from the surface valleys which have Fermi surfaces allowing low-energy scattering. The existence of mid-gap states is a necessary by-product of the topology of the gapped Dirac points described by Hamiltonians of the form in Eq. 2. The essential effect of the DW on the electrons is that Δ_i changes sign as one moves through it. This means the Chern number evolves from $-1/2$ on one side of the DW to $1/2$ on the other, introducing gapless states bound to the DW interior [18]. At the critical temperature T_c where the transition occurs, one expects DW's to proliferate, opening a channel for conduction which is absent below T_c . This could lead to singular behavior (e.g., a cusp) in the conductivity at the transition [50, 51], and should also have a signature when the surface is probed via tunneling. A further possibility to probe the physics is by looking for differences in conductivity between field-cooling and zero-field cooling of the system through its critical temperature. The latter leads to nucleation of groundstate domains with random orientation, and DW's between them, which cannot relax on the time scale of an experiment. Thus one expects stronger surface conduction from a zero field-cooled sample [16, 52, 53]. Finally, the presence of charged DW's on the surface might be detected directly via coupling to electro-magnetic waves [54], whose scattering should be sensitive to the proliferation of DW's.

In summary, the surface of a magnetically-doped TCI hosts magnetic ordering in the topological state even when the bulk is disordered. The unique electronic structure of a TCI surface leads to a richer set of possible ordered states than would be expected from time-reversal symmetry protected topological insulators, and implies a number of unusual physical behaviors.

Acknowledgements – The authors thank Fernando de Juan for helpful comments, and U. Nitzsche for technical assistance. This work was supported by the NSF through Grant Nos. DMR-1506263 and DMR-1506460, by the US-Israel Binational Science Foundation, and by MEyC-Spain under grant FIS2015-64654-P. Computations were carried out on the ITF/IFW and IU Karst clusters. HAF also thanks the Aspen Center for Physics where some of this work was performed.

-
- [1] L. Fu, Phys. Rev. Lett. **106**, 106802 (2011).
- [2] J. Liu, W. Duan, and L. Fu, Phys. Rev. B **88**, 241303(R) (2013).
- [3] T. Hsieh, H. Lin, J. Liu, W. Duan, and L. Fu, Nat. Comm. **3**, 982 (2012).
- [4] Y. Tanaka, Z. Ren, T. Sato, K. Nakayama, S. Souma, T. Takahashi, K. Segawa, and Y. Ando, Nat. Phys. **8**, 800 (2012).
- [5] S.-Y. Xu, C. Liu, N. Alidoust, M. Neupane, D. Qian, I. Belopolski, J. D. Denlinger, Y. J. Wang, H. Lin, L. A. Wray, et al., Nat. Comm. **3**, 1192 (2012).
- [6] P. Dziawa, B. J. Kowalski, K. Dybko, R. Buczko, A. Szczerbakow, M. Szot, E. Lusakowska, T. Balasubramanian, B. M. Wojek, M. H. Berntsen, et al., Nature Materials. **11**, 1023 (2012).
- [7] Y. Okada, M. Serbyn, H. Lin, D. Walkup, W. Zhou, C. Dhital, M. Neupane, S. Xu, Y. J. Wang, R. Sankar, et al., Science **341**, 6153 (2013).
- [8] C. Yan, J. Liu, Y. Zang, J. Wang, Z. Wang, P. Wang, Z.-D. Zhang, L. Wang, X. Ma, S. Ji, et al., Phys. Rev. Lett. **112**, 186801 (2014).
- [9] Q. Liu, C. Liu, C. Xu, X. Qu, and S. Zhang, Phys. Rev. Lett. **102**, 156603 (2009).
- [10] R. R. Biswas and A. V. Balatsky, Phys. Rev. B **81**, 233405 (2010).
- [11] I. Garate and M. Franz, Phys. Rev. B **81**, 172408 (2010).
- [12] D. Abanin and D. Pesin, Phys. Rev. Lett. **106**, 136802 (2011).
- [13] C.-X. Liu, B. Roy, and J. D. Sau, Phys. Rev. B **94**, 235421 (2016).
- [14] D. Efimkin and V. Galitski, Phys. Rev. B **89**, 115431 (2014).
- [15] J. Shen and J. J. Cha, Nanoscale **6**, 14133 (2014).
- [16] B. A. Assaf, F. Katmis, P. Wei, C.-Z. Chang, B. Satpati, J. S. Moodera, and D. Heiman, Phys. Rev. B **91**, 195310 (2015).
- [17] F. Zhang, X. Li, J. Feng, C. Kane, and E. Mele, arXiv:1309.7682.
- [18] C. Fang, M. J. Gilbert, and B. A. Bernevig, Phys. Rev. Lett. **112**, 046801 (2014).
- [19] Y. Ando and L. Fu, Annu. Rev. Condens. Matter Phys. **6**, 361 (2015).
- [20] Z. Li, S. Shao, N. Li, K. McCall, J. Wang, and S. X. Zhang, Nano Letters **13**, 5443 (2013).
- [21] A. A. Taskin, F. Yang, S. Sasaki, K. Segawa, and Y. Ando, Phys. Rev. B **89**, 121302 (2014).
- [22] J. Shen, Y. Jung, A. S. Disa, F. J. Walker, C. H. Ahn, and J. J. Cha, Nano Letters **14**, 4183 (2014).
- [23] P. B. Littlewood, B. Mihaila, R. K. Schulze, D. J. Sarik, J. E. Gubernatis, A. Bostwick, E. Rotenberg, C. P. Opeil, T. Durakiewicz, J. L. Smith, et al., Phys. Rev. Lett. **105**, 086404 (2010).
- [24] R. Jackiw and C. Rebbi, Phys. Rev. D **13**, 3398 (1976).
- [25] See Online Supplementary Material.
- [26] C.-X. Liu, X.-L. Qi, H. Zhang, X. Dai, Z. Fang, and S.-C. Zhang, Phys. Rev. B **82**, 045122 (2010).
- [27] P. G. Silvestrov, P. W. Brouwer, and E. G. Mishchenko, Phys. Rev. B **86**, 075302 (2012).
- [28] L. Brey and H. A. Fertig, Phys. Rev. B **89**, 084305 (2014).
- [29] M. Inoue, K. Ishii, and T. Tatsukawa, J. Low Temp. Phys. **23**, 785 (1975).
- [30] M. Inoue, K. Ishii, and H. Yagi, J. Phys. Soc. Japan **43**, 903 (1977).
- [31] M. Inoue, T. Tanabe, H. Yagi, and T. Tatsukawa, J. Phys. Soc. Japan **47**, 1879 (1979).
- [32] T. Story, R. R. Galazka, R. B. Frankel, and P. A. Wolff, Phys. Rev. Lett. **56**, 777 (1986).
- [33] G. Karczewski, J. K. Furdyna, D. L. Partin, C. N. Thrush, and J. P. Heremans, Phys. Rev. B **46**, 13331 (1992).
- [34] F. Geist, H. Pascher, N. Frank, and G. Bauer, Phys. Rev. B **53**, 3820 (1996).
- [35] F. Geist, W. Herbst, C. Mejía-García, H. Pascher, R. Rupprecht, Y. Ueta, G. Springholz, G. Bauer, and M. Tacke, Phys. Rev. B **56**, 13042 (1997).
- [36] A. Prinz, G. Brunthaler, Y. Ueta, G. Springholz, G. Bauer, G. Grabecki, and T. Dietl, Phys. Rev. B **59**, 12983 (1999).
- [37] A. Lusakowski, A. Jędrzejczak, M. Górka, V. Osiniy, M. Arciszewska, W. Dobrowolski, V. Domukhovskii, B. Witkowska, T. Story, and R. R. Galazka, Phys. Rev. B **65**, 165206 (2002).
- [38] T. Dietl, C. Śliwa, G. Bauer, and H. Pascher, Phys. Rev. B **49**, 2230 (1994).
- [39] J. Liu, C. Fang, and L. Fu, arXiv:1604.03947 (2016).
- [40] G. Rosenberg and M. Franz, Phys. Rev. B **85**, 195119 (2012).
- [41] M. Lasia and L. Brey, Phys. Rev. B **86**, 045317 (2012).
- [42] I. Fulga, N. Avraham, H. Beidenkopf, and A. Stern, Phys. Rev. B **94**, 125405 (2016).
- [43] T. Wehling, A. Black-Schaffer, and A. Balatsky, Adv. Phys. **76**, 1 (2014).
- [44] L. Brey, H. A. Fertig, and S. Das Sarma, Phys. Rev. Lett. **99**, 116802 (2007).
- [45] Precise results for the stiffnesses are provided in the Supplementary Material.
- [46] M. F. Paulos, S. Rychkov, B. C. van Rees, and B. Zan, Nuc. Phys. B **902**, 246 (2016).
- [47] R. Rajaraman, *Solitons and Instantons* (North-Holland, New York, 1989).
- [48] J. V. José, L. P. Kadanoff, S. Kirkpatrick, and D. R. Nelson, Phys. Rev. B **16**, 1217 (1977).
- [49] A. Schaakel, *Boulevard of Broken Symmetries* (World Scientific, 2008).
- [50] T. Jungwirth and A. H. MacDonald, Phys. Rev. Lett. **87**, 216801 (2001).
- [51] K. Dhochak, E. Shimshoni, and E. Berg, Phys. Rev. B **91**, 165107 (2015).
- [52] K. Ueda, J. Fujioka, B.-J. Yang, J. Shiogai, A. Tsukazaki, S. Nakamura, S. Awaji, N. Nagaosa, and Y. Tokura, Phys. Rev. Lett. **115**, 056402 (2015).
- [53] Z. Tian, Y. Kohama, T. Tomita, H. Ishizuka, T. H. Hsieh, J. J. Ishikawa, K. Kindo, L. Balents, and S. Nakatsuji, Nat. Phys. **12**, 134 (2016).
- [54] E. Y. Ma, Y.-T. Cui, K. Ueda, S. Tang, K. Chen, N. Tamura, P. M. Wu, J. Fujioka, Y. Tokura, and Z.-X. Shen, Science **350**, 538 (2015).

Supplementary information for “Surface Magnetism in Topological Crystalline Insulators”

Sahinur Reja¹, H.A.Fertig¹, L. Brey² and Shixiong Zhang¹

¹Department of Physics, Indiana University, Bloomington, IN 47405

² Instituto de Ciencia de Materiales de Madrid, (CSIC), Cantoblanco, 28049 Madrid, Spain

I. BULK HAMILTONIAN

Our analysis begins with a tight-binding model [?] for materials in the (Sn,Pb)Te class, which is a rocksalt

structure, i.e. an fcc lattice with a two sublattices, such that atomic species alternate among the points of a simple cubic lattice. The Hamiltonian of the system is given by $H_{bulk} = H_m + H_{nn} + H_{nnn} + H_{so}$, with

$$\begin{aligned} H_m &= \sum_j m_j \sum_{\mathbf{R},s} \vec{c}_{j,s}^\dagger(\mathbf{R}) \cdot \vec{c}_{j,s}(\mathbf{R}), \\ H_{nn} &= t \sum_{(\mathbf{R},\mathbf{R}'),s} \vec{c}_{a,s}^\dagger(\mathbf{R}) \cdot \vec{d}_{\mathbf{R},\mathbf{R}'} \vec{d}_{\mathbf{R},\mathbf{R}'} \cdot \vec{c}_{b,s}(\mathbf{R}') + h.c., \\ H_{nnn} &= \sum_j t'_j \sum_{((\mathbf{R},\mathbf{R}')),s} \vec{c}_{j,s}^\dagger(\mathbf{R}) \cdot \vec{d}_{\mathbf{R},\mathbf{R}'} \vec{d}_{\mathbf{R},\mathbf{R}'} \cdot \vec{c}_{j,s}(\mathbf{R}') + h.c., \\ H_{so} &= i \sum_j \lambda_j \sum_{\mathbf{R},s,s'} \vec{c}_{j,s}^\dagger(\mathbf{R}) \times \vec{c}_{j,s'}(\mathbf{R}) \cdot (\vec{\sigma})_{s,s'}. \end{aligned} \quad (S1)$$

In these equations \mathbf{R} labels the sites of a cubic lattice, $j = a, b$ are the species type (Sn/Pb or Te), which have on-site energies $m_{a,b}$, and $s = \uparrow, \downarrow$ is the electron spin. The 3-vector of operators $\vec{c}_{j,s}(\mathbf{R})$ annihilates electrons in p_x, p_y and p_z orbitals, and there is a local spin-orbit coupling strength λ_j on each site. ($\vec{\sigma}$ is the vector of Pauli matrices.) The vectors $\vec{d}_{\mathbf{R},\mathbf{R}'}$ are unit vectors pointing from \mathbf{R} and \mathbf{R}' , and, finally, the sum over $(\mathbf{R}, \mathbf{R}')$ denotes positions which are nearest neighbors, while $((\mathbf{R}, \mathbf{R}'))$ denotes next nearest neighbors.

At an L point, it is possible to diagonalize H_{bulk} analytically. These eigenvalues are $E_{0,j} = 4t'_j - \lambda_j + m_j$, $E_{\pm,j} = -2t'_j + \lambda_j/2 \pm R_j + m_j$, with $R_j \equiv \sqrt{144t_j'^2 + 24t'_j\lambda_j + 9\lambda_j^2}/2$, with $j = a, b$ each of these three values being doubly degenerate. For large enough m , the lowest eigenvalue for the b sites approaches the highest eigenvalue for the a sites, and we can construct a projected 4×4 Hamiltonian representing states with energies $E \sim E_{+,a} \sim E_{-,b}$ which is valid for \mathbf{k} near an L point. This projected Hamiltonian is conveniently written in terms of states which have well-defined quantum numbers upon $2\pi/3$ rotation around a $\Gamma - L$ direction. For example, for the L point $\mathbf{k}_1 \equiv (\frac{\pi}{2}, \frac{\pi}{2}, \frac{\pi}{2})$, we define states

$$|m, s, j\rangle \equiv \frac{1}{\sqrt{3}} \left[|p_x, j\rangle + w^m |p_y, j\rangle + w^{2m} |p_z, j\rangle \right] \otimes |s\rangle$$

where $|p_{x(y,z)}, j\rangle$ is a $p_{x(y,z)}$ -orbital on a site of type j , $|s = \pm\rangle$ is a spin state with quantization axis parallel to \mathbf{k}_1 , and $w = e^{2\pi i/3}$. The relevant eigenstates of the Hamiltonian are then

$$\begin{aligned} |1, j\rangle &= -u_j w |m=0, s=+, j\rangle + v_j |m=2, s=-, j\rangle, \\ |2, j\rangle &= u_j w^* |m=0, s=-, j\rangle + v_j |m=1, s=+, j\rangle, \end{aligned} \quad (S2)$$

with

$$\begin{aligned} u_j &= \frac{\sqrt{2}\lambda_j}{\sqrt{(8t'_j + \varepsilon_j)^2 + 2\lambda_j^2}}, \\ v_j &= \frac{8t'_j + \varepsilon_j}{\sqrt{(8t'_j + \varepsilon_j)^2 + 2\lambda_j^2}}, \end{aligned} \quad (S3)$$

$\varepsilon_a = -2t'_a + \lambda_a/2 + R_a$, and $\varepsilon_b = -2t'_b + \lambda_b/2 - R_b$. Note under a $2\pi/3$ rotation around the (111) direction, $|1, j\rangle \rightarrow e^{-i\pi/3}|1, j\rangle$ and $|2, j\rangle \rightarrow e^{i\pi/3}|2, j\rangle$.

To proceed, we form the \mathbf{k} -dependent bulk Hamiltonian $H_b(\mathbf{k}) = e^{-i\mathbf{k}\cdot\mathbf{R}} H_{bulk} e^{i\mathbf{k}\cdot\mathbf{R}}$ which acts on states of definite crystal momentum \mathbf{k} , and project this into the 4×4 space defined by the states in Eq. S2. Writing $\mathbf{k} = \mathbf{k}_1 + \mathbf{q}$, for small q one finds, after considerable algebra and up to an overall constant,

$$\bar{H}_1 = Aq_3\tau_x - B[q_1\tilde{\sigma}_2 + q_2\tilde{\sigma}_1]\tau_y + [m + C_{12}^{(-)}(q_1^2 + q_2^2) + C_3^{(-)}q_3^2]\tau_z + C_{12}^{(+)}(q_1^2 + q_2^2) + C_3^{(+)}q_3^2. \quad (S4)$$

In this expression, $\tilde{\sigma}_1 \equiv \frac{\sqrt{3}}{2}\sigma_x - \frac{1}{2}\sigma_y$ and $\tilde{\sigma}_2 \equiv \frac{\sqrt{3}}{2}\sigma_y + \frac{1}{2}\sigma_x$ are 2×2 matrices acting on the 1,2 indices of the basis states (Eq. S2), and τ_x, τ_y, τ_z are standard Pauli matrices acting on the sublattice index. The coefficients in Eq. S4 are explicitly given by $A = -2\sqrt{3}(u_a u_b + v_a v_b)$, $B = \sqrt{6}(-u_a v_b + v_a u_b)$, $C_{12}^{(\pm)} = \frac{1}{2}[(C_a - D_a/2) \pm (C_b - D_b/2)]$, and $C_3^{(\pm)} = -\frac{1}{2}(D_a \pm D_b)$, with $C_j = 2t'_j(\frac{1}{3} + u_j^2 - v_j^2)$ and $D_j = 8t'_j/3$. Finally, the wavevector coordinates (q_1, q_2, q_3) are given in terms of the wavevector components of \mathbf{q} by

$$\begin{pmatrix} q_1 \\ q_2 \\ q_3 \end{pmatrix} = \begin{pmatrix} \frac{1}{\sqrt{2}} & -\frac{1}{\sqrt{2}} & 0 \\ \frac{1}{\sqrt{6}} & \frac{1}{\sqrt{6}} & -\frac{2}{\sqrt{3}} \\ \frac{1}{\sqrt{3}} & \frac{1}{\sqrt{3}} & \frac{1}{\sqrt{3}} \end{pmatrix} \begin{pmatrix} q_x \\ q_y \\ q_z \end{pmatrix}.$$

Eq. S4 is essentially equivalent to previously derived results based on the symmetry of the underlying Hamiltonian [?], but the quadratic terms follow from the microscopic model and play an important role in determining the coupling to surface magnetic degrees of freedom which are the focus of this study. Note that the matrix $\tilde{\sigma}_1$ carries out a mirror reflection which is a symmetry of

H_{bulk} .

Analogous approximate forms for H_{bulk} near the other three L points can be obtained by appropriate symmetry operations: the states and effective Hamiltonian in the vicinity of $\mathbf{k}_4 \equiv (\frac{\pi}{2}, \frac{\pi}{2}, -\frac{\pi}{2})$ are related to Eqs. S2 and S4 by a mirror reflection across the $x - y$ plane, and these quantities for the other two L points can be constructed by $2\pi/3$ rotations around the (111) direction from those of \mathbf{k}_4 . For example, for the \mathbf{k}_4 point we denote the mirror operation by M_z , and note the fact that $H_{bulk}(k_x, k_y, -k_z) = M_z H_{bulk}(k_x, k_y, k_z) M_z^{-1}$. Writing $\mathbf{k} = \mathbf{k}_4 + \mathbf{q}'$, one finds a long-wavelength form for $H_{bulk}(\mathbf{k})$ in the vicinity of \mathbf{k}_4 , \bar{H}_4 , which is formally the same form as Eq. S4, but with the caveat that the $\tilde{\sigma}_i$ operators act on the mirror reflected states $|1, j\rangle_4 \equiv M_z|1, j\rangle$ and $|2, j\rangle_4 \equiv M_z|2, j\rangle$, and $\mathbf{q} \rightarrow \mathbf{q}'$ with

$$\begin{pmatrix} q'_1 \\ q'_2 \\ q'_3 \end{pmatrix} = \begin{pmatrix} \frac{1}{\sqrt{2}} & -\frac{1}{\sqrt{2}} & 0 \\ \frac{1}{\sqrt{6}} & \frac{1}{\sqrt{6}} & -\frac{2}{\sqrt{3}} \\ \frac{1}{\sqrt{3}} & \frac{1}{\sqrt{3}} & \frac{1}{\sqrt{3}} \end{pmatrix} \begin{pmatrix} q_x \\ q_y \\ q_z \end{pmatrix}.$$

Rewriting \bar{H}_4 in terms of \mathbf{q} , one finds

$$\begin{aligned} \bar{H}_4 = & A(\eta q_2 + q_3)\tau_x - B[q_1\tilde{\sigma}'_2 + (q_2 + \eta q_3)\tilde{\sigma}'_1]\tau_y + \left\{ m + C_{12}^{(-)}[q_1^2 + (q_2 + \eta q_3)^2] + C_3^{(-)}(q_2 + \eta q_3)^2 \right\} \tau_z \\ & + C_{12}^{(+)}[q_1^2 + (q_2 + \eta q_3)^2] + C_3^{(+)}(q_2 + \eta q_3)^2, \end{aligned} \quad (\text{S5})$$

with $\eta = 2\sqrt{2}/3$. \bar{H}_1 and \bar{H}_4 may be used to construct surface states and effective surface Hamiltonians, as described in the next section.

II. SURFACE HAMILTONIANS

As discussed in the main text, when the mass of the system is negative ($m < 0$) the energy bands described by \bar{H}_1 near the \mathbf{k}_1 point are topological, and we expect that surfaces will host gapless states [?]. These must be eigenstates of \bar{H}_1 , \bar{H}_4 , or of one of the Hamiltonians associated with \mathbf{k}_2 or \mathbf{k}_3 , but with $q_3 \rightarrow i\kappa$ in order to make the state evanescent in the bulk. Focusing on \mathbf{k}_1 , we set $q_1 = q_2 = 0$ to find surface states exactly at the $\bar{\Gamma}$ point. The evanescent state must satisfy

$$\left[i\kappa A\tau_x + \left(m - C_3^{(-)}\kappa^2 \right) \tau_z \right] |\kappa\rangle = \left(E + C_3^{(+)}\kappa^2 \right) |\kappa\rangle. \quad (\text{S6})$$

Note that arriving at this equation is only possible because we have retained quadratic terms in \bar{H}_1 [? ? ?]. In order to satisfy Eq. S6, κ must obey

$$\left(E + C_3^{(+)} \right)^2 = \left(m - C_3^{(-)}\kappa^2 \right)^2 - A^2\kappa^2. \quad (\text{S7})$$

For a given value of E , one finds two values of κ^2 that satisfy Eq. S7, κ_{\pm}^2 . With the proper choice of overall

sign for κ_{\pm} , the eigenstates $|\kappa_{+}\rangle$ and $|\kappa_{-}\rangle$ vanish in real space deep in the bulk of the system, but generically neither vanishes at the surface. However if $|\kappa_{+}\rangle \propto |\kappa_{-}\rangle$, we can form a linear combination of these that does [? ? ?]. One may show that for $\text{sgn}(mC_3^{(-)}) < 0$, there is a unique value of E for which this is possible, given by $E = E_{\bar{\Gamma}} \equiv -\frac{C_3^{(+)}}{C_3^{(-)}}m$. Because the states $|\kappa_{\pm}\rangle$ have no dependence on the $\tilde{\sigma}_i$ operators (see Eq. S6), we can form two independent pairs of these.

The Dirac point states for the \bar{M} points is obtained in a very analogous way. For example, starting with \bar{H}_4 (Eq. S5), we make the replacement $q_3 \rightarrow i\kappa$ and set $q_1 = q_2 = 0$. One may find two different values of κ with the same eigenvectors of \bar{H}_4 at the energy $E_{\bar{M}} = -m\frac{C_{12}^{(+)}\eta^2 + C_3^{(+)}}{C_{12}^{(-)}\eta^2 + C_3^{(-)}}$. Thus we can construct two states meeting the boundary conditions. From the rotational symmetry, each of the other \bar{M} points will host a pair of degenerate states at precisely this energy, yielding three sets of Dirac points. Note that $E_{\bar{M}} \neq E_{\bar{\Gamma}}$, so the Dirac points are at two different energies, in agreement with numerical tight-binding studies [?].

To simplify subsequent discussion, we drop the particle-hole symmetry-breaking terms (i.e., set $C_{12}^{(+)}, C_3^{(+)} = 0$) in \bar{H}_1 , \bar{H}_4 , and the long-wavelength Hamiltonians for the other L points, except to note that

the surface Dirac point energies at the $\bar{\Gamma}$ and \bar{M} points

are different, so that we add $E_{\bar{\Gamma}}$ and $E_{\bar{M}}$ to \bar{H}_1 and \bar{H}_4 , respectively. Thus we make the replacements

$$\begin{aligned}\bar{H}_1 &\rightarrow Aq_3\tau_x - B[q_1\tilde{\sigma}_2 + q_2\tilde{\sigma}_1]\tau_y + [m + C_{12}^{(-)}(q_1^2 + q_2^2) + C_3^{(-)}q_3^2]\tau_z + E_{\bar{\Gamma}}, \\ \bar{H}_4 &\rightarrow A(\eta q_2 + q_3)\tau_x - B[q_1\tilde{\sigma}'_2 + (q_2 + \eta q_3)\tilde{\sigma}'_1]\tau_y + \left\{m + C_{12}^{(-)}[q_1^2 + (q_2 + \eta q_3)^2] + C_3^{(-)}(q_2 + \eta q_3)^2\right\}\tau_z + E_{\bar{M}}.\end{aligned}\quad (\text{S8})$$

These Hamiltonians are next projected into space of surface states derived above. The explicit form of these that are relevant for the $\bar{\Gamma}$ point (with effective Hamiltonian \bar{H}_1) are

$$\begin{aligned}|u_1\rangle &= \frac{1}{\sqrt{2}} \begin{pmatrix} 1 \\ 0 \\ -i\text{sgn}(A) \\ 0 \end{pmatrix} \mathcal{N}_z (e^{-\kappa+z} - e^{-\kappa-z}), \\ |u_2\rangle &= \frac{1}{\sqrt{2}} \begin{pmatrix} 0 \\ 1 \\ 0 \\ -i\text{sgn}(A) \end{pmatrix} \mathcal{N}_z (e^{-\kappa+z} - e^{-\kappa-z}).\end{aligned}$$

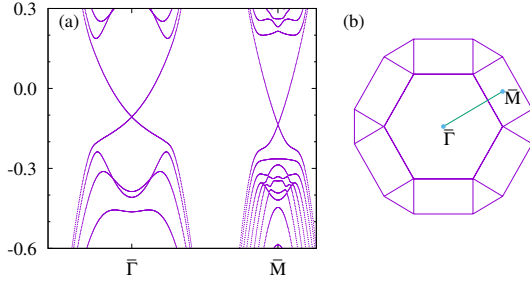


FIG. 1. (Color online.) The Bnad structure along $\bar{\Gamma}$ to \bar{M} points showing the Dirac cones on (111) surface. The parameter values are mentioned in the text.

In these expressions, the four entries are coefficients of the $(|1,a\rangle, |2,a\rangle, |1,b\rangle, |2,b\rangle)$ states at the \mathbf{k}_1 point, z denotes the direction perpendicular to the surface (with $z > 0$ being points inside the system), \mathcal{N}_z is a normalization constant, and $\kappa_{\pm}^2 = m + [A^2 \pm \sqrt{4mC_3^{(-)}A^2 + A^4}]/2C_3^{(-)}$. Note that the wavefunctions have equal weight on the two sublattices, and moreover are eigenstates of the $\tilde{\sigma}_3$ operator. The corresponding results for the \mathbf{k}_4 point may also be written as eigenstates of the relevant $\tilde{\sigma}_3$ operator (i.e., acting on states near the \mathbf{k}_4 point), and also have equal weight on the two sublattices, although the relative phase is more complicated and has the form

$$e^{i\theta_4} \equiv \frac{A - i\eta B}{\sqrt{A^2 + \eta^2 B^2}}.$$

With the explicit surface wavefunctions in hand it is straightforward to project \bar{H}_1 and \bar{H}_4 onto the space of

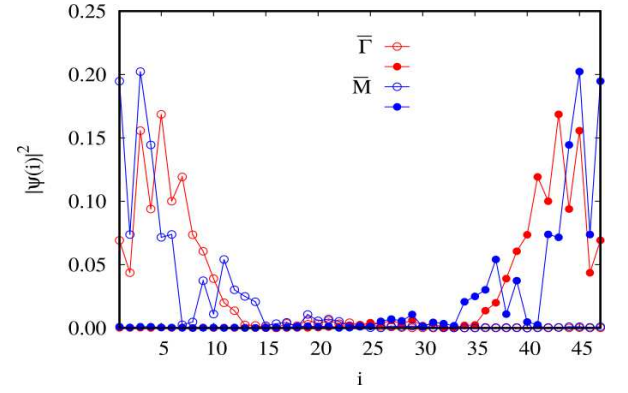


FIG. 2. (Color online.) Surface state wave function weights $|\psi(i)|^2$ as a function of layer indexed by i , stacked along (111) direction. The results are shown for a slab with 47 layers. The red (blue) circles indicate states associated with the $\bar{\Gamma}$ (\bar{M}) point of the surface Brillouin zone. Open (closed) circles indicate states associated with the top (bottom) surface of the slab.

surface states, yielding surface Hamiltonians for the $\bar{\Gamma}$ and \bar{M} points. These take the form

$$H_{\bar{\Gamma}} \equiv B[q_1\tilde{\sigma}_2 + q_2\tilde{\sigma}_1] + E_{\bar{\Gamma}} \quad (\text{S9})$$

and

$$H_{\bar{M}} \equiv \frac{AB}{\sqrt{A^2 + \eta^2 B^2}} [(\eta^2 - 1)q_2\tilde{\sigma}_1 + q_1\tilde{\sigma}_2] + E_{\bar{M}}. \quad (\text{S10})$$

Note that the states which the $\tilde{\sigma}_i$ operators act upon in $H_{\bar{M}}$ are different than those of $H_{\bar{\Gamma}}$. Analogous results may be obtained for the other two \bar{M} points by $2\pi/3$ rotations of Eq. S10.

As described in the main text, we assume that there are impurity spins which order ferromagnetically on the surface, and treat these in mean-field theory, so that they form an effective uniform Zeeman field that couples to the electron spin operators, projected onto the surface states, as shown in Eq. 1 in the main text. Adding these to the various Hamiltonians (e.g., Eqs. S9 and S10) leads to the generic Hamiltonian in Eq. 2 of the main text.

III. NUMERICAL METHODS

We numerically simulate the model Hamiltonian given in Eq. S1 for (Sn,Pb)Te materials. As we mentioned above, the lattice structure is fcc with two sublattices a and b (i.e., a rocksalt structure). Our numerical studies focus on the (111) surface, so that it is convenient to view the fcc lattice as stacked, two-dimensional triangular lattices, i.e., a close packed structure, with ABC stacking. Triangular layers of the a and b sublattices are arranged alternately along the stacking direction.

The electronic structure calculations we report are done by taking a finite but relatively large number of these layers along (111) direction (i.e., a slab geometry). We used 47 layers which we found to be sufficient to avoid interaction of states of the two slab surfaces. The model parameters we used in Eq. S1 for the surface state calculations are $t = 0.9$, $t'_a = -t'_b = -0.5$, $\lambda_a = \lambda_b = -0.7$, $m_a = -m_b = 3.5$. These place the system in the topological regime, as can be seen from the band structure of the slab, shown in Fig. 1, which demonstrate the presence of gapless states in the bulk gap around the $\bar{\Gamma}$ and \bar{M} points in the surface Brillouin zone. It is important to note that the energy of the Dirac point at $\bar{\Gamma}$ is slightly higher than that of \bar{M} . This asymmetry is responsible for some of the unusual magnetic behaviors described in the main text.

The confinement of wavefunctions with energies in the bulk gap to the surfaces can be demonstrated explicitly. If we consider states with crystal momenta precisely at the $\bar{\Gamma}$ and \bar{M} points, one finds two pairs of states for each, with each pair associated with one of the two slab surfaces. Fig. 2 shows the electron density associated with representative states for each of the high symmetry points on the surfaces. From direct examination we see that the surface states penetrate approximately 10 layers into the system bulk for the parameters we use.

As mentioned in the main text, we have modeled the coupling of the electrons to magnetic impurities by an $s-d$ model. In real systems these will be randomly located (on a single sublattice) at different depths from the surface, but on average the coupling of the spins to both states should be the same for both the $\bar{\Gamma}$ and \bar{M} points. To model this, we use the information of the wave functions shown in Fig. 2 by putting magnetic moments on *two* layers, say L_1, L_2 , near each surface. We then choose effective local Zeeman fields on each layer of magnitudes

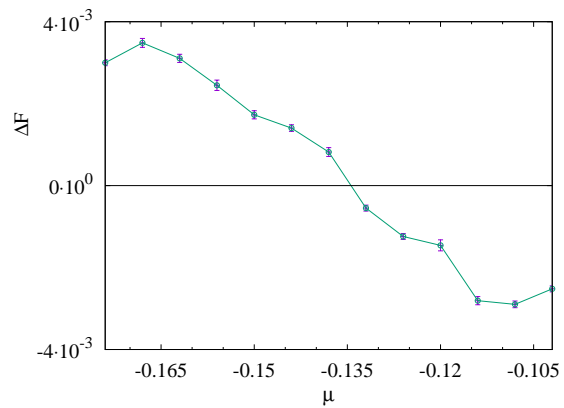


FIG. 3. (Color online.) Average difference in free energy per surface atom [in units of t] as a function of chemical potential for $J|\vec{s}| = 0.2$ when magnetic moments are oriented in (111) and $(11\bar{1})$ directions. Results are for 30 random locations of two impurities on a -sublattice sites, within five layers of the surface. The average difference is qualitatively similar to the array of impurities discussed in the main text. Standard deviation is shown as error bars.

$(J|\vec{s}|)_{L_1}$ and $(J|\vec{s}|)_{L_2}$ such that they satisfy the equation

$$\frac{(J|\vec{s}|)_{L_1}}{(J|\vec{s}|)_{L_2}} = \frac{|\psi_{\bar{\Gamma}}(L_2)|^2 - |\psi_{\bar{M}}(L_2)|^2}{|\psi_{\bar{M}}(L_1)|^2 - |\psi_{\bar{\Gamma}}(L_1)|^2}. \quad (\text{S11})$$

This guarantees that the net coupling of the impurity spins to electron spins in the $\bar{\Gamma}$ and \bar{M} states will have the same overall strength. In practice, in our calculations the magnetic impurities reside on layer 3 and 5 near one surface and on layer 43 and 45 near the other.

IV. RANDOM IMPURITY COUPLING TO SURFACE ELECTRONS

In the main text we discussed the physics when the coupling of the magnetic impurities to surface electron is uniform. But in real materials, this coupling could be randomly distributed, particularly because the magnetic impurities are on random locations among the a -sublattice sites. To check the effect of this randomness, we simulate the system 30 times, putting two magnetic impurities (dilute limit) at two random a -sublattice sites within five layers of the system surface. (The top layer of the supercell is illustrated in the inset of Fig. 2 of the main text.) Then we calculate the average and standard deviation for the difference in free energy as a function of chemical potential when magnetic moments are aligned parallel to the 111 and $11\bar{1}$ directions respectively. Fig. 3 shows that the energy difference goes from positive to negative in a manner and at a scale very similar to the behavior illustrated in the main panel of the Fig. 2 of the main text. This suggests that disorder in the coupling between the magnetic impurities and the surface electrons does not change the qualitative behavior of the physics of this system.

V. SPIN STIFFNESS COEFFICIENTS

In this section, we describe our computation of the spin stiffness for a fully filled band. For simplicity we consider an isotropic surface Dirac cone, as is found for the $\bar{\Gamma}$ point; anisotropic Dirac cones (\bar{M} points) should yield qualitatively similar results. Our generic Hamiltonian has the form

$$H_0 = \alpha [(q_x + b_x)\sigma_x + (q_y + b_y)\sigma_y + b_z\sigma_z],$$

where for simplicity of notation we have rewritten the parameter Δ_i in the text as αb_z . Eigenstates of H_0 are

spinors of the form

$$\begin{pmatrix} u \\ v \end{pmatrix}_p = \frac{e^{i\mathbf{q}\cdot\mathbf{r}}}{\mathcal{S}^{1/2}\sqrt{q'^2 + (p\varepsilon_0(\mathbf{q}) - b_z)^2}} \begin{pmatrix} q'_x - iq'_y \\ p\varepsilon_0(\mathbf{q}) - b_z \end{pmatrix} \equiv |\mathbf{q}, p\rangle,$$

where $p = \pm 1$ is the band index for states with energy $p\varepsilon(\mathbf{q}) = p\sqrt{q_x'^2 + q_y'^2 + b_z^2}$, $(q'_x, q'_y) = (q_x + b_x, q_y + b_y)$, and \mathcal{S} is the area of the surface. We consider the effect on the total electronic energy of a filled lower band ($p = -1$) of adding a spatially varying component to \mathbf{b} , of the form $h = \delta\vec{b} \cdot \vec{\sigma} \cos \mathbf{Q} \cdot \mathbf{r}$ to H_0 , focusing on its dependence on \mathbf{Q} for small Q . Using second order perturbation theory, one finds for the energy shift $\delta E(\mathbf{Q})$ that

$$\begin{aligned} \delta E(\mathbf{Q}) - \delta E(0) &\approx \frac{1}{32} \sum_{\mu, \nu=x,y} Q_\mu Q_\nu \sum_{\mathbf{q}} \left\{ \frac{|\langle \mathbf{q}, -1 | \delta\vec{b} \cdot \vec{\sigma} | \mathbf{q}, +1 \rangle|^2}{\varepsilon_0(\mathbf{q})^2} \partial_\mu \partial_\nu \varepsilon_0(\mathbf{q}) - \frac{1}{\varepsilon_0(\mathbf{q})} \partial_\mu \partial_\nu |\langle \mathbf{q}, -1 | \delta\vec{b} \cdot \vec{\sigma} | \mathbf{q}, +1 \rangle|^2 \right\} \\ &\equiv \frac{\mathcal{S}}{2} \sum_{\mu, \nu=x,y} \rho_{\mu, \nu} Q_\mu Q_\nu. \end{aligned} \tag{S12}$$

With a lengthy albeit in principle straightforward calculation, the coefficients $\rho_{\mu, \nu}$ may all be computed explicitly, with the results

$$\begin{aligned} \rho_{xx} &= \frac{2}{\pi\Delta^{(0)}} \left[\frac{2}{5} \alpha^2 \delta b_x^2 + \frac{8}{15} \alpha^2 \delta b_y^2 + \frac{4}{15} \alpha^2 \delta b_z^2 \right], \\ \rho_{yy} &= \frac{2}{\pi\Delta^{(0)}} \left[\frac{8}{15} \alpha^2 \delta b_x^2 + \frac{2}{5} \alpha^2 \delta b_y^2 + \frac{4}{15} \alpha^2 \delta b_z^2 \right], \\ \rho_{xy} &= \frac{2}{\pi\Delta^{(0)}} \left[\frac{8}{15} \alpha^2 \delta b_x \delta b_y \right], \end{aligned}$$

where $\Delta^{(0)} = \alpha b_z$ is the gap for the unperturbed spectrum of H_0 .